High-latitude Joule heating response to IMF inputs

M. McHarg, F. Chun, and D. Knipp
Department of Physics, United States Air Force Academy, Colorado, USA

G. Lu and B. Emery
High Altitude Observatory, NCAR, Boulder, Colorado, USA

A. Ridley
Space Physics Research Laboratory, University of Michigan, Ann Arbor, Michigan, USA

Received 2 December 2004; revised 2 June 2005; accepted 7 June 2005; published 27 August 2005.

[1] We evaluate the response of the high-latitude Joule heating to orientation and magnitude of the interplanetary magnetic field (IMF). Approximately 9000 individual Joule heating patterns derived from data assimilation for the northern hemisphere were used to develop averaged and hemispherically integrated Joule power maps for the northern hemisphere north of 40° magnetic latitude. Hemispherically integrated Joule heating increases with IMF magnitude when the IMF is southward, but is relatively unchanged with increased IMF magnitude when the IMF is north. Only a small IMF B_y effect is evident in the Joule heating patterns. We quantify the IMF effects with linear fits of integrated Joule heating as a function of IMF magnitude for eight different IMF clock angle bins in the GSM Y-Z plane. During extreme northward IMF conditions, Joule heating is restricted to the high latitude dayside. During extreme southward IMF conditions, Joule heating is located predominantly in the auroral region, with increased heating in the morning sector compared to the evening sector. This additional heating may lead to the increased incidence of gravity waves reported in the morning sector. Our estimate of the increase of hemispherically integrated Joule heating with IMF magnitude during southward IMF periods is 13GW/nT.

Citation: McHarg, M., F. Chun, D. Knipp, G. Lu, B. Emery, and A. Ridley (2005), High-latitude Joule heating response to IMF inputs, *J. Geophys. Res.*, *110*, A08309, doi:10.1029/2004JA010949.

1. Introduction

[2] Joule heating is one of the three important energy inputs into the Earth's ionosphere along with extreme ultraviolet radiation and charged particle precipitation. Electrodynamic coupling of the magnetosphere and ionosphere is mainly through the interactions of the three-dimensional current system and the associated electric fields. The energy input due to Joule heating is the manifestation of the ohmic interaction of the ionospheric part of these currents and the electric field. During active geomagnetic periods the Joule heating can be as large as 50% of the total energy input into the ionosphere [*Knipp et al.*, 2004]. Even during less active periods, Joule heating still exhibits the most variability in the ionospheric energy budget [*Knipp et al.*, 2004].

[3] Understanding how ionospheric Joule heating responds to changes in the interplanetary magnetic field (IMF) is important to understanding the basic coupling mechanisms between the magnetosphere and the ionosphere. This understanding is in turn fundamental to quantifying space weather effects such as atmospheric drag on low earth-orbiting satellites and high-latitude ionospheric scintillation on technological systems. The goal of this study is to parameterize the height-integrated ionospheric Joule heating at high-latitudes as a function of IMF magnitude for eight different IMF orientations.

[4] To develop average and standard deviation Joule heating patterns, we assembled data from many Assimilative Mapping of Ionospheric Electrodynamics (AMIE) event studies into a large database. The AMIE procedure is described by *Richmond and Kamide* [1988]. Briefly, the procedure assimilates a diverse set of ground- and space-based observations in a least- squares sense onto a spatial grid covering magnetic latitudes above 40°. In locations where data do not exist, the procedure reverts to climatology. The AMIE procedure produces maps of the relevant electrodynamic quantities. Among these are maps of Joule heating. These maps serve as the basis for our work. All Joule heating data for this study were obtained from the northern hemisphere only.

[5] This database contains over 15,000 individual patterns derived from over 50 days of high-time resolution observations. Table 1 of *Chun et al.* [2002] shows the intervals contained within the database, along with a brief description of the type of event (i.e., high speed stream, coronal mass ejection or slow flow). As they discuss, this

0148-0227/05/2004JA010949

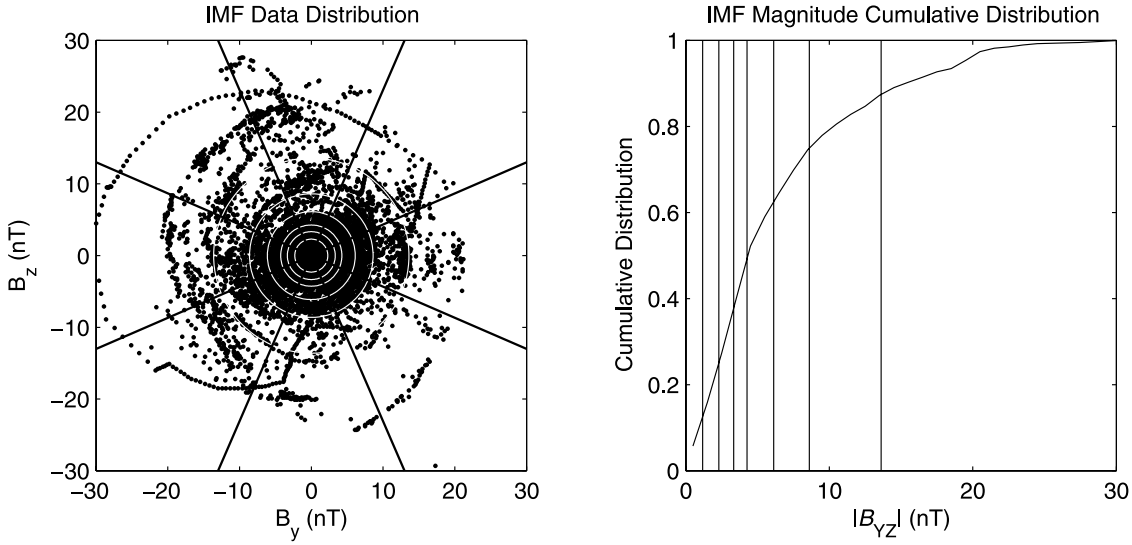

Figure 1. Distribution of IMF measurements for all the events used in this study. The left panel of Figure 1 shows the distribution of events in the GSM By-Bz plane. Each point represents the IMF value for one of the patterns. Superimposed over the distribution are eight clock angle sectors and eight concentric octile magnitude rings. The right panel shows the cumulative distribution of the IMF magnitudes in the GSM Y-Z plane, with vertical lines superimposed at each octile. Figure 1 demonstrates that we have a representative distribution of events in terms of IMF clock angle and magnitude.

database gives a representative coverage of all the major flow types found within the solar wind.

2. Data and Analysis

[6] Approximately 9000 of the individual Joule heating patterns have associated IMF measurements (appropriately shifted to the arrival time at the magnetosphere). These patterns were used to establish the Joule heating response to IMF variations. The left panel of Figure 1 shows the distribution of these data in the GSM Y-Z plane. The patterns have a reasonably isotropic distribution in the IMF Y-Z plane. Superimposed on the IMF data are eight equally spaced angle bins used in this analysis. Overlaying the data are concentric rings representing constant IMF magnitude. These magnitudes have been selected so that each ring contains equal numbers of points. The right panel of Figure 1 shows the cumulative distribution of IMF data as a function of IMF magnitude in the Y-Z plane. For this paper we use the transverse components only of the magnetic field to determine IMF magnitude: $|B_{trans}| = \sqrt{B_y^2 + B_z^2}$. The 50% level is at a magnitude of approximately 5 nT. The octiles shown as concentric rings in the left panel of Figure 1 are also shown as vertical lines in the right panel of Figure 1. Included in the distribution are patterns derived during periods of low, moderate, and high geomagnetic activity.

[7] Each data point in Figure 1 has an associated spatially distributed Joule heating pattern represented by a two-dimensional 24 × 24 matrix. The matrix grid size is 2° in magnetic latitude (mlat) by one hour magnetic local time (MLT). The height-integrated Joule heating (with units of W/m^2) is calculated by $JH = \Sigma_p E^2$, where Σ_p is the Pedersen conductance, and E is the magnitude of the electric field in the rotating frame of the earth for each bin. Joule heating usually maximizes around 120 km where the Pedersen conductivity peaks [*Richmond et al.*, 1976]. The AMIE-derived Pedersen conductance estimates combined effects of both solar and auroral particle ionization.

[8] The AMIE algorithm does not directly include the effects of neutral wind, so the neutral wind dynamo is not explicitly included in the electrodynamic calculations for the magnitude of the electric field [*Richmond and Thayer*, 2000]. Including the neutral wind can change the Joule heating by 10–30% in the dawn, dusk and polar cap [*Thayer et al.*, 1995]; with localized reductions up to 40%, and enhancements of up to 400% during intervals when the neutral winds are steady [*Thayer*, 1998]. In a two-day study period *Lu et al.* [1995], using the AMIE procedure in combination with the thermosphere-ionosphere general circulation model (TIGCM), found the neutral winds reduced the Joule heating by 28%. The AMIE algorithm also neglects heating due to electric fields with scale sizes less than about π times the grid size [*Matsuo et al.*, 2003]. *Codrescu et al.* [2000] show that these small scale variations contribute roughly the same amount as the average electric field to the ionospheric Joule heating. For this study these smallest scale sizes are 500 km.

[9] Figure 2 shows the dramatic difference in hemispherically integrated Joule heating between IMF north ($+B_z$) and south ($-B_z$) conditions. In the left column of Figure 2 we present all events within ±22.5° of the north and south IMF clock angles in the GSM Y-Z plane, and plot the integrated Joule heating versus IMF Y-Z magnitude. The top left panel of Figure 2 also has the IMF magnitude octiles marked as vertical lines. During southward IMF ($-B_z$) periods, the Joule heating increases with IMF magnitude, as does the amount of scatter in the data. On the other hand, for

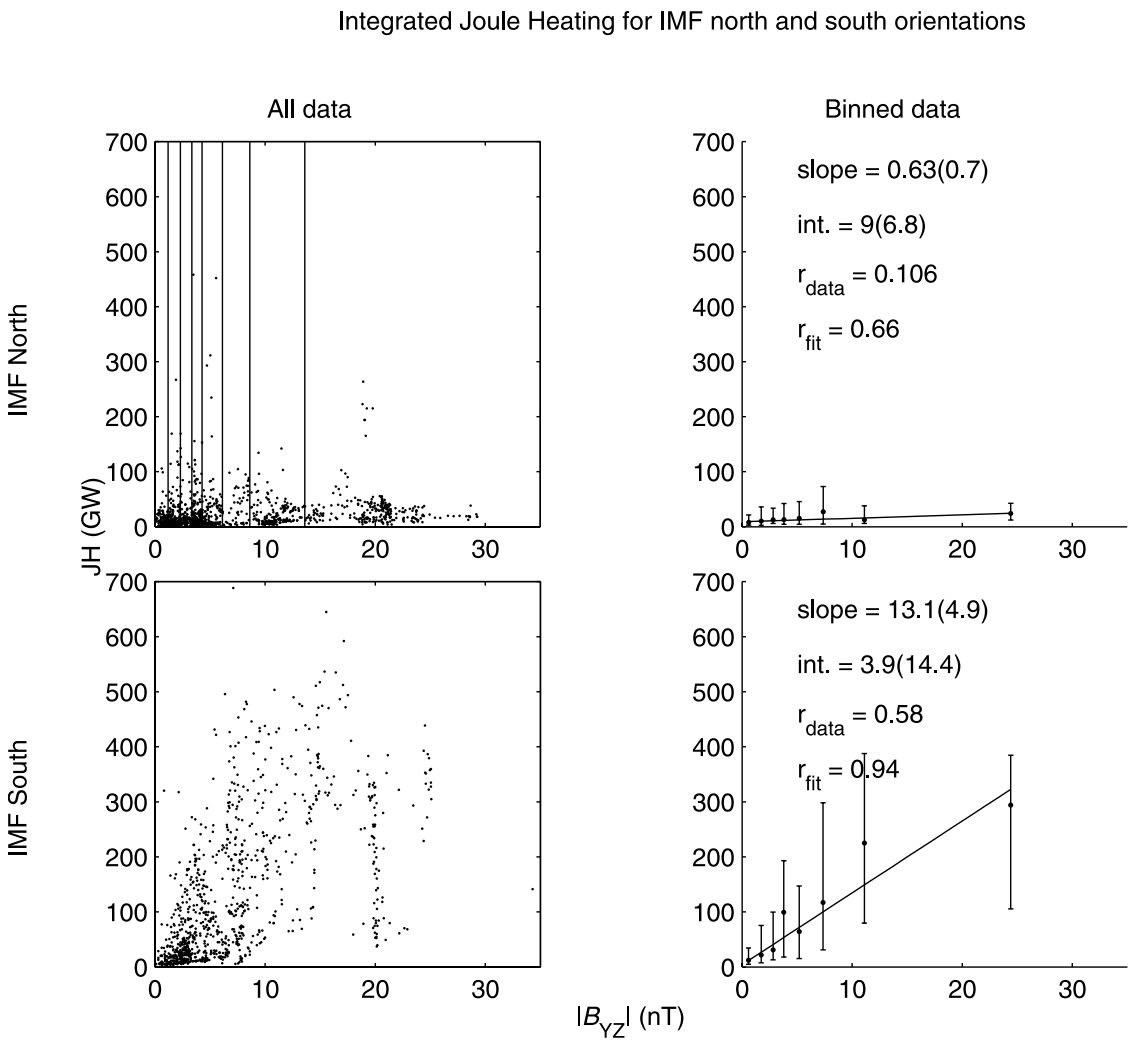

Figure 2. Hemispherically integrated Northern Hemisphere Joule heating in GW over the northern polar cap for northward and southward IMF periods. The left column of Figure 2 shows all the data points found in the northward and southward IMF clock angle sectors defined in the left panel of Figure 1. Within the subpanels the magnitude of the hemispherically integrated Joule heating is plotted on the ordinate, and the magnitude of the corresponding Y-Z magnitude is plotted on the abscissa. The northward (top left subpanel) has the IMF octiles found from Figure 1 superimposed over the data. The right column of subpanels in Figure 2 shows the results of binning the data by IMF magnitude. The median of the Joule heating data within each bin is shown at the center of the bin, along with the 15th and 85th percentiles of the Joule heating found in that bin. Linear fits of the Joule heating to the binned data are shown as solid lines in the right panels, along with the fit coefficients and uncertainties above the fits. Note that during periods of northward IMF there is very little response to changes in the IMF magnitude, while periods of southward IMF exhibit a generally linear increase in Joule heating with IMF magnitude.

northward IMF ($+B_z$), there is little increase in integrated Joule heating with increased IMF magnitude, and there is less scatter in the data.

[10] To better quantify these differences we created bins of IMF magnitude consistent with the octiles in Figure 1. We then analyzed the statistical distribution of values within each IMF magnitude bin. The results are shown in the right column of Figure 2. The horizontal position of these binned data is taken from the centers of the octiles described in Figure 1. The right column of panels in Figure 2 shows only the median value of the integrated Joule heating centered in each IMF magnitude bin, along with the 15th and 85th percentiles of the Joule heating within that bin. The distribution of integrated Joule heating values within each bin is frequently non-Gaussian, as indicated by the nonsymmetric nature of the error bars with respect to the median values. Because of this non-Gaussian distribution, we chose to report the median and 15–85th percentiles rather than the mean and standard deviations associated with each bin.

[11] Binning the data in this manner allows us to determine a linear fit between the Joule heating and IMF magnitude for each IMF clock angle. While there is no a

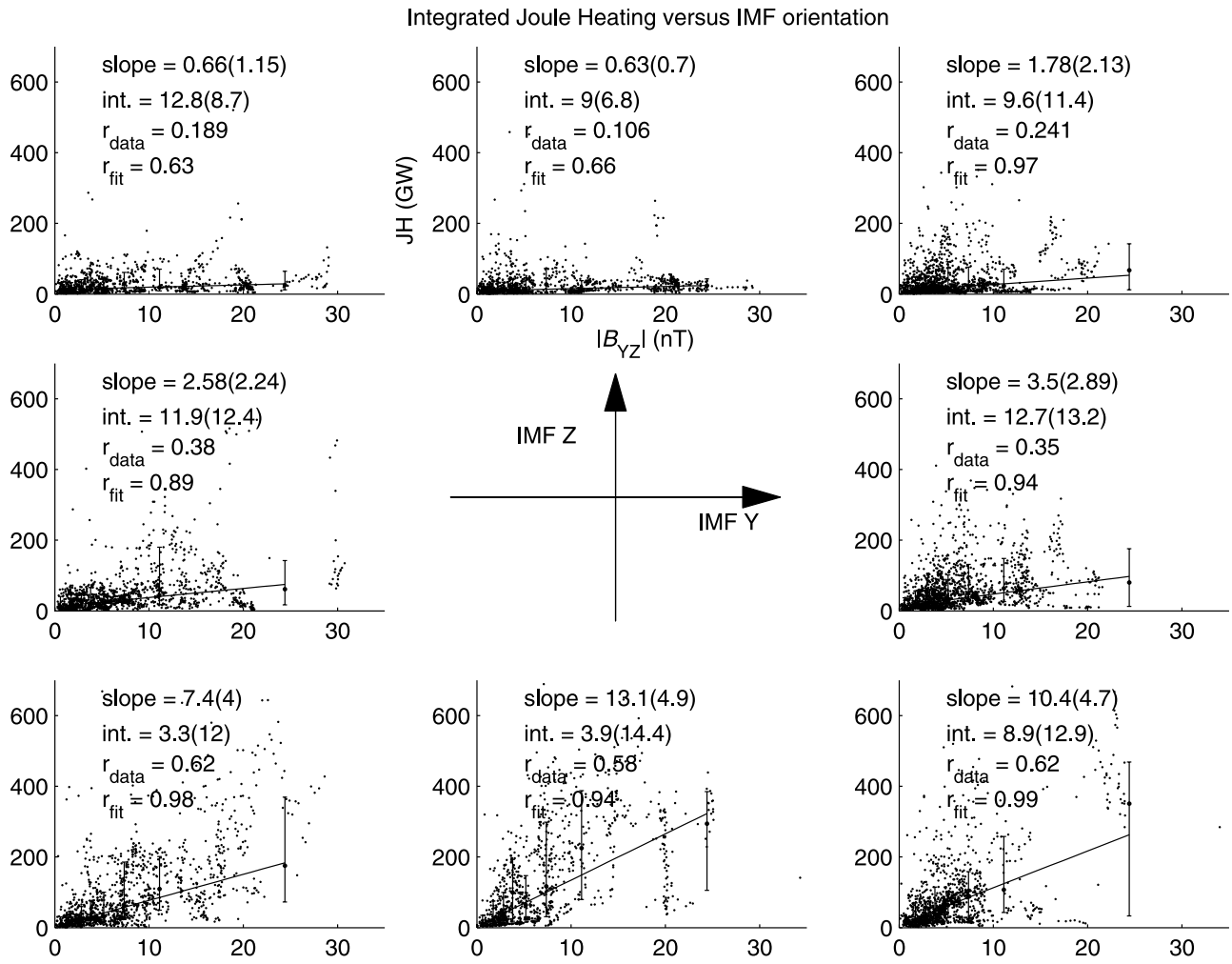

Figure 3. Hemispherically integrated Northern Hemisphere Joule heating in GW over all eight clock angle bins described in Figure 1. The data have been binned by IMF magnitude as in Figure 2, with a weighted, linear fit applied to the median values within the bin. The resulting fit parameters are shown for each fit along with the uncertainties in the fit parameters. Again note that for IMF north there is little increase in Joule heating when the IMF magnitude is increased. Conversely, greater IMF magnitude is associated with larger Joule heating during IMF southward periods.

priori reason to choose a linear fit, the data seem consistent with this simple relation. These linear fits were obtained by using only the median Joule heating values at the centers of the bins. For each median value we establish a symmetric variance of σ_i = (85th percentile − 15th percentile)/2. We do this for two reasons. First, it allows us to determine a weighted linear fit between the Joule heating and IMF magnitude. Second, it allows us to determine the variance in the fitted coefficients using the method of *Press et al.* [1990].

[12] Shown in the right column of Figure 2 are the fit coefficients with the slope in *GW*/*nT*, and the intercept in *GW*. The associated variance in each fit coefficient is shown in parentheses. The linear correlation coefficient calculated for the entire set of IMF magnitudes and Joule heating data is shown in the right hand column of Figure 2 as r_{data}. In addition the linear correlation coefficient between the center values of the eight IMF magnitude and the median values of the Joule heating is shown in the right column as r_{fit}. In all cases r_{fit} is substantially larger than r_{data} since the Joule heating values used in computing the correlation coefficient tend to lie more along a line for the median values in r_{fit}. This means that the fit using the IMF magnitude may predict the mean value of the Joule heating reasonably well, but is essentially useless in predicting individual values.

[13] The trends in the fitted data match that of the individual data shown in the left column of Figure 2. These trends indicate that using the binned data with symmetric error bars to establish the fit coefficients is reasonable, based on the data at hand.

[14] Figure 3 shows the results of a similar analysis for eight IMF clock angle bins. The three subpanels with IMF ($+B_z$) show a slope of less than 2 *GW*/*nT*, with the predominately northward IMF ($+B_z$) subpanel having the smallest slope of 0.63 ± 0.7 *GW*/*nT*. In marked contrast the three subpanels with IMF ($-B_z$) have slopes between 7.7 and 13 *GW*/*nT*, with the southward IMF ($-B_z$) group having the largest slope of 13.1 ± 4.9 *GW*/*nT*. This indicates that the ionospheric Joule heating is tied to the increased convection electric fields and particle-enhanced conductivity associated

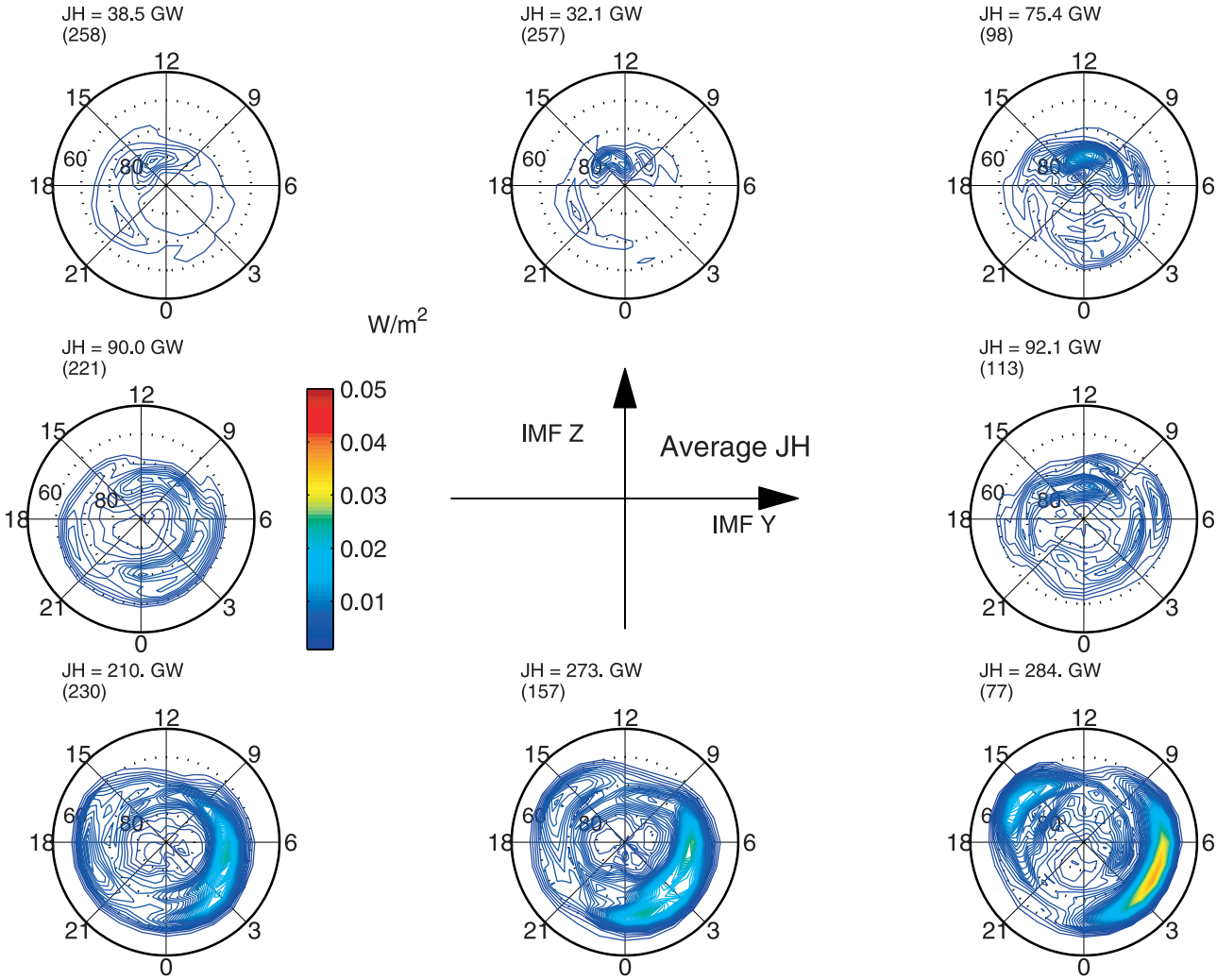

Figure 4. Spatial distribution of the height-integrated Northern Hemisphere Joule heating (W/m^2) in the northern ionosphere as a function of IMF clock angle during periods of $|B| > 13.9$ nT. One dial plot is shown for each of the 8 clock angle bins described in Figures 1 and 2. In each dial plot the Joule heating is shown from 50° to the pole in magnetic latitude and local time coordinates. Magnetic midnight is at 00 hours on the clock dial, dawn at 06, magnetic noon at 12, and dusk at 18 hours. Above each dial plot is a number in parenthesis which denotes the number of patterns used in this clock angle and IMF magnitude bin to make the average shown in the dial plot. The integrated Joule heating across the polar cap for the average is shown in Giga Watts. Note that GSM $+B_y$ is to the right, and GSM $+B_z$ is up in the clock angle plots. IMF B_z north (the top row) shows most of the Joule heating constrained to the high latitude dayside cusp region. During periods of IMF B_z, south (the bottom row) heating is increased around the auroral oval, with more heating on the dawn side.

with IMF ($-B_z$) conditions. Note the increased spread in the 15th and 85th percentiles for the IMF southward sectors.

[15] The second trend evident in Figure 3 is the similarity in the intercepts of the linear fits to Joule heating. This low level background of heating is consistent with a constant background of activity irrespective of the IMF orientation.

[16] The spatial distributions of Joule heating versus IMF with $|B_{trans}| > 13.9$ nT are shown in Figure 4. Each element of Figure 4 contains a magnetic latitude-local time plot showing the northern hemisphere from 40° magnetic latitude to the pole. Magnetic local times are shown, with magnetic midnight at 00, dawn at 06, noon at 12, and dusk at 18. Each subpanel contains the average of all events within each of the eight angle bins shown in Figure 2 and having IMF magnitude greater than 13.9 nT. The integrated Joule heating patterns for the northern hemisphere are shown above each subpanel, along with the total number of individual patterns contained within the average (in parentheses). All Joule heating patterns are shown on a common intensity scale with 30 contours spaced evenly between 0.0–.05 W/m^2.

[17] Figure 4 shows a significant difference in the statistical response of Joule heating between IMF $+B_z$ and $-B_z$ conditions. During $+B_z$ conditions most of the heating is in the high-latitude dayside portion of the ionosphere, with little heating around the auroral oval. The hemispherically integrated Joule heating is relatively small, typically 30–75 GW. Such high-latitude dayside heating was reported

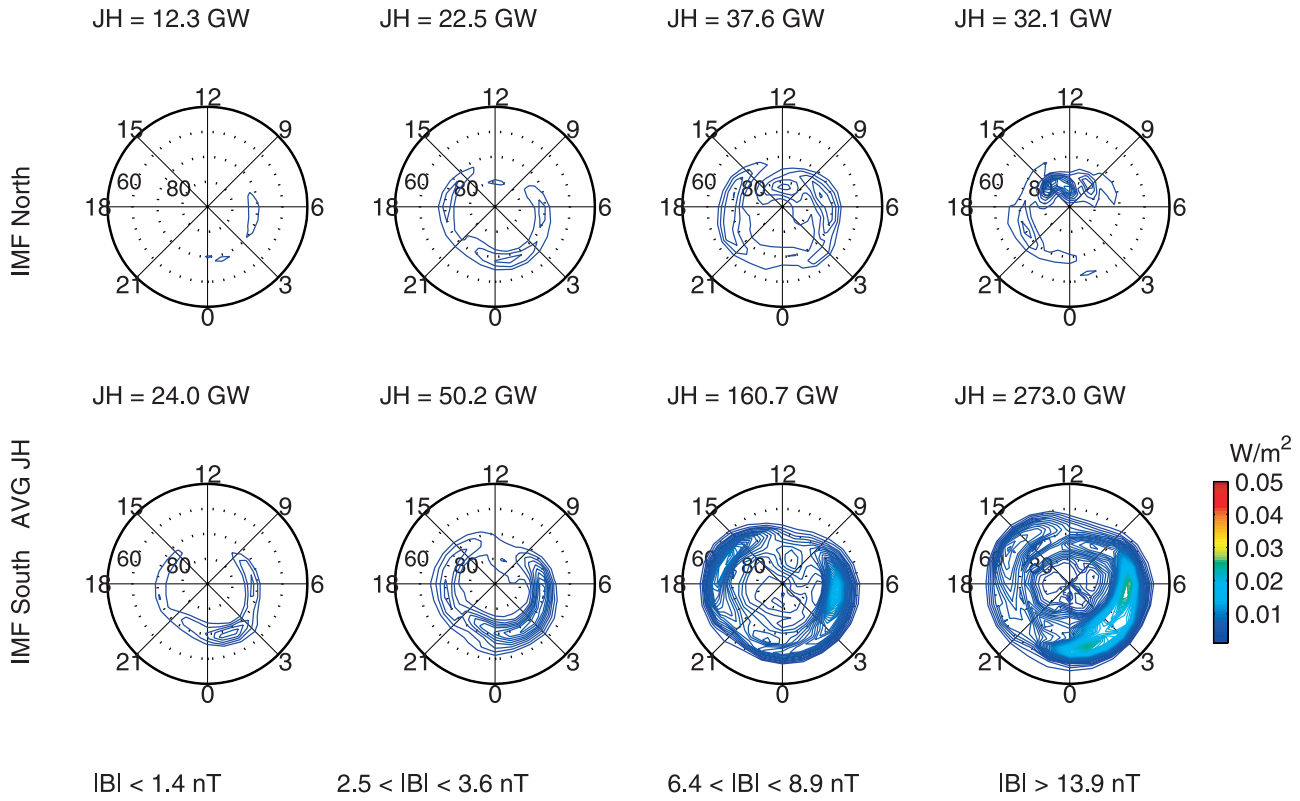

Figure 5. Spatial height-integrated Northern Hemisphere Joule heating for IMF pure north and south as a function of $|B|$. The top row of dial plots are the pure north case, and the bottom row are for the pure south case. IMF magnitude increases to the right in these dial plots. Note: the far right plots are the IMF north and south shown in Figure 4. Notice for B_z north as the IMF magnitude increases, the integrated Joule heating (number above each dial plot) stays approximately constant. This agrees with the results shown in Figure 3. For IMF south, the integrated Joule heating increases with increasing IMF magnitude, again in agreement with the results of Figure 3.

by *Chun et al.* [2002] during intervals of negative polar cap index (PCI). The two IMF $+B_y$ and $-B_y$ subpanels show slightly increased heating with the heating spread uniformly around the auroral oval. The $-B_z$ orientations reveal increased heating around the oval, with all three B_y subpanels showing an increase in heating between approximately midnight and 06 MLT and between 60° and 70° magnetic latitude. The $+B_y - B_z$ (lower right) subpanel also shows increased heating in the afternoon region between 14–17 MLT in the auroral latitudes. The integrated Joule heating values rise during $-B_z$ conditions to over 200 GW, consistent with the data shown in Figure 3.

[18] Figure 5 shows the evolution of Joule heating with IMF magnitude for the northward IMF ($+B_z$) and southward ($-B_z$) orientations. The top row in Figure 5 shows the northward IMF ($+B_z$) Joule heating as a function of IMF magnitude, while the bottom row shows the Joule heating for the same magnitudes for southward IMF ($-B_z$) conditions. The elements on the right of Figure 5 are the same as the north and south IMF subpanels shown in Figure 4, and they have the same intensity scale.

[19] The top row of Figure 5, from left to right, shows that the Joule heating during IMF ($+B_z$) conditions evolves in both configuration and magnitude. Very little heating is present when the IMF magnitude is small. Stronger IMF ($+B_z$) conditions produce heating around a presumed high-latitude auroral oval at approximately 70° which expands equatorward to approximately 65° with additional forcing. Under very strong IMF ($+B_z$) forcing there is increased heating on the dayside as previously discussed. In contrast, the bottom row of Figure 5 shows Joule expanding equatorward with increased IMF ($-B_z$) magnitude. Under the strongest forcing, the majority of the heating is at approximately 60° mlat, with the pronounced dawn/dusk asymmetry noted in Figure 4.

3. Discussion and Conclusions

[20] *Foster et al.* [1983] created the first global Joule heating estimates by combining AE-C satellite electric-field drift meter data with particle and solar conductance estimates. They showed increased heating in the cleft, dusk, and dawn regions, which are similar with our results shown in Figures 3 and 4.

[21] *Rich et al.* [1987] estimated Joule heating using data collected from the polar orbiting DMSP/F7 satellite. Using a statistical database of 7 days (90 orbits), *Rich et al.* [1987] found the height integrated Joule heating in the auroral premidnight auroral zone was a few milli-watts per square meter, in good agreement with our data. Additionally *Rich et al.* [1987] also show a marked increase in Joule heating on the high latitude dayside southern hemisphere iono-

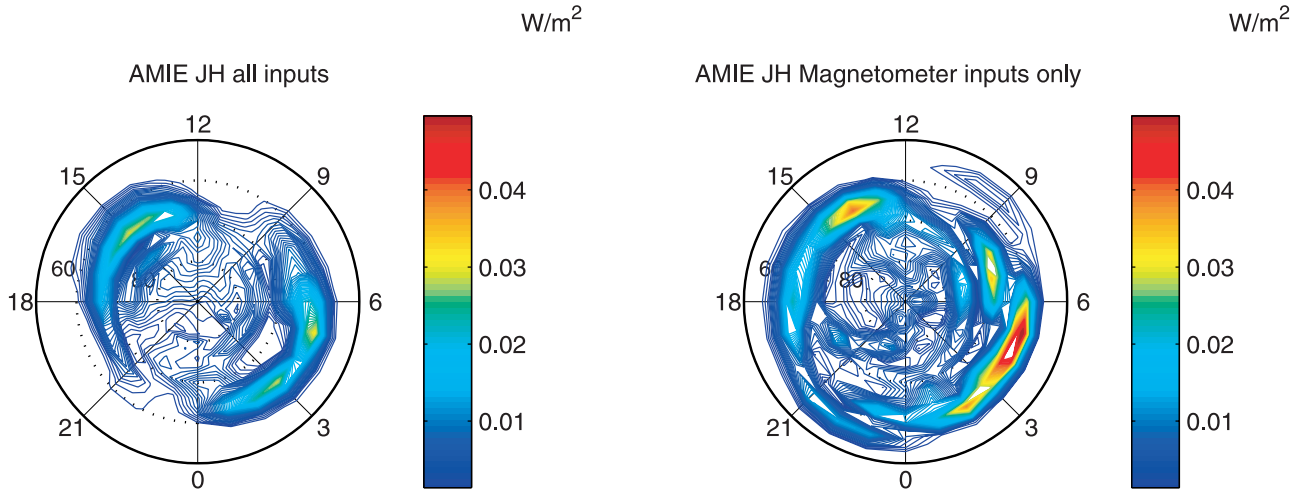

Figure 6. Comparison of Joule heating patterns for the period 15 May 1997, 11:10 UT, using two different methods of AMIE reconstruction during a period of strongly southward IMF conditions. The left panel of the figure is derived with all data sources included in the AMIE reconstruction, while the right panel of the figure shows the same pattern using only ground based magnetometer data included. Both patterns show a distinct assymetery, with larger Joule heating in the postmidnight sector of the auroral oval.

sphere. This increased Joule heating is consistent with our data for IMF northward conditions shown in our Figure 4.

[22] *Chun et al.* [2002] reported increased Joule heating on the high-latitude dayside during periods when PCI was negative. Our study clearly shows this enhanced dayside heating during intervals of $+B_z$ values (Figure 4) and supports the *Chun et al.* [2002] contention that this heating is indicative of lobe reconnection. They also reported that the high-latitude heating was due mainly to enhancements of the high-latitude dayside electric field rather than conductivity increases.

[23] *Matsuo et al.* [2003] used measurements of plasma drifts from the Dynamics Explorer (DE) 2 satellite to estimate the electric field and electric field variability in magnetic latitude and MLT bins as a function of IMF parameters. They found the polar average of the root mean square (RMS) electric field increased by a factor of two during IMF ($-B_z$) conditions when the IMF transverse magnetic field amplitude $|B_{trans}|$ rose from $|B_{trans}| < 4$ nT to $|B_{trans}| > 7$ nT. Our estimate of a linear rise in the hemispherically integrated Joule heating of 13 GW/nT (see Figure 3) is consistent with their reports of increasing RMS electric field in the polar cap. We would expect the Joule heating to increase as $|E|^2$ if the conductance stays constant.

[24] During southward IMF ($-B_z$) conditions, *Matsuo et al.* [2003] found a maximum in the RMS of the electric field magnitude at 72° mlat and 06 MLT. Figure 4 shows that with strongly forced IMF ($-B_z| > 13.6$ nT) conditions, a maximum in the Joule heating occurs at approximately 65° and 03–04 MLT. For periods with $6.4 < |B_{trans}| < 8.9$ nT, we find a maximum in the Joule heating pattern at approximately the same latitude and local time as the maximum in the RMS electric field reported by *Matsuo et al.* [2003] (see our Figure 5). For northward IMF, *Matsuo et al.* [2003] found a maximum in the RMS electric field on the high-latitude dayside at 81° mlat and 12 MLT. Figure 5 shows a maximum in the Joule heating at the same location for $6.4 < |B_{trans}| < 8.9$ nT. This maximum in the high-latitude dayside Joule heating during IMF ($+B_z$) conditions increases with increasing B_{trans}.

[25] *Matsuo et al.* [2003] found that the maximum on the high-latitude dayside RMS electric field was dominated by small-scale electric field variability. This suggests the high-latitude dayside Joule heating during northward IMF ($+B_z$) may be due to the variable electrodynamic conditions routinely observed inside the cusp in both ground-based magnetometer, radar and satellite-based electric field measurements [*McHarg et al.*, 1995; *Ables et al.*, 1998; *Baker et al.*, 1990, 1995; *André et al.*, 2000, 1988; *Maynard et al.*, 1991; *André et al.*, 1990].

[26] During periods with $-B_z$ orientation, Joule heating is more prevalent around the nightside auroral oval. The bottom row of Figure 5 also shows a general increase in Joule heating with increased IMF magnitude. These results are consistent with *Weimer* [2001], who shows increased electric field strength around the auroral oval during periods with IMF $-B_z$. We show stronger heating in the morning sector compared to the premidnight sector of the auroral oval during periods of large IMF magnitude.

[27] The distinct asymmetry between the premidnight and postmidnight side Joule heating is a consistent feature in our data base. The early morning sector is very dynamic in terms of particle precipitation and electric field variability. Both of these factors may give rise to additional heating in the postmidnight-to-dawn sector. It is also possible that the enhanced Joule heating in this region is an artifact of the sparcity of satellite sampling. The current fleet of low-earth orbiting satellites do not sample this area. The AMIE procedure heavily relies on ground magnetometer data for estimates of electric field and conductivity in the 00 UT–06 UT region.

[28] To investigate this possibility we compared the results of AMIE patterns derived using all inputs versus those found when using ground based magnetometers only. Figure 6 shows the comparison of the two AMIE patterns the time period 15 May 1997, 11:10 UT as a representative

Table 1. Integrated Joule Heating Linear Fit Coefficients and Uncertainties

IMF Clock Angle (+CW from +Z)	Slope (Slope Uncertainty)/Intercept (Intercept Uncertainty)
67.5° to 112.5°	*JH* (*GW*) = 3.5 (2.89)|*B*(*nT*)| + 12.7 (13.2)
22.5° to 67.5°	*JH* (*GW*) = 1.78(2.13)|*B*(*nT*)| + 9.6 (11.4)
−22.5° to 22.5°	*JH* (*GW*) = 0.63 (0.7)|*B*(*nT*)| + 9 (6.8)
−67.5° to −22.5°	*JH* (*GW*) = 0.66 (1.15)|*B*(*nT*)| + 12.8 (8.7)
−112.5° to −67.5°	*JH* (*GW*) = 2.58 (2.24)|*B*(*nT*)| + 11.9 (12.4)
−157.5° to −112.5°	*JH* (*GW*) = 7.4 (4.0)|*B*(*nT*)| + 3.3 (12)
−157.5° to 157.5°	*JH* (*GW*) = 13.1 (4.9)|*B*(*nT*)| + 3.9 (14.4)
112.5° to 157.5°	*JH* (*GW*) = 10.4 (4.7)|*B*(*nT*)| + 8.9 (12.9)

test case during strong Southward IMF conditions. The left panel shows the AMIE pattern from our database which includes satellite, radar and ground-based magnetometer input. The right panel of Figure 6 shows the same pattern derived using ground based magnetometers only. Detailed comparisons between the two data sets is beyond the scope of this paper, but while differences in the patterns are observable, both reveal the same strong asymmetry between the premidnight and postmidnight side of the auroral oval.

[29] Examination of electrodynamic patterns (not shown here) reveal this premidnight/postmidnight asymmetry in Joule heating is due mainly to the Pedersen conductance, and due less to the electric field. The increased Pedersen conductance in the postmidnight sector is in turn due to an increased energy flux of incoming auroral electrons in the postmidnight sector. *Hardy et al.* [1985] show a similar asymmetric auroral particle energy flux (postmidnight enhancement) during periods with $Kp > 6-$. *Fuller-Rowell and Evans* [1987] do not show this asymmetry in the auroral energy flux when the hemispherical power input due to particles is 61–91 GW. Measurements by *Shue et al.* [2001] reveal a very similar strong asymmetry of the auroral brightness in the Lyman-Birge-Hopfield (LBH) long bands of the N_2 emission spectra in the ultraviolet portion of the spectrum during periods of strongly southward IMF. Since LBH long emission is approximately proportional to the total precipitating electron energy flux [*Germany et al.*, 1994], we believe the measurements of *Shue et al.* [2001] are in substantial agreement with our proposition that an increased electron energy flux in the postmidnight hours during strongly southward IMF conditions causes a strongly asymmetric Joule heating pattern.

[30] One result of Joule heating in the ionosphere is production of gravity waves in the neutral atmosphere [*Richmond*, 1978; *Roble et al.*, 1978]. Observations from the DE-2 satellite showed greatly increased vertical neutral winds in the dawn sector when the Auroral Electrojet index was greater than 500 nT (see Figure 8 of *Innis and Conde* [2002]). They interpret their measurements as possible evidence of polar cap gravity waves with a source in the midnight-dawn auroral oval. We believe the enhanced Joule heating during periods of strong IMF forcing, as shown in Figure 4, may be a source of these polar cap gravity waves. In addition to gravity waves, auroral infrasonic waves have an increased probability of occurrence around 06 MLT, and such waves are commonly associated with intense particle precipitation and Joule heating in the electrojets [*Wilson*, 1969; *Wilson et al.*, 1976].

[31] In summary we find the hemispherically integrated Joule heating is strongly dominated by IMF polarity. The relationship between integrated Joule heating and IMF magnitude for eight different clock angles is summarized in Table 1. In this table the clock angle is positive measured clockwise from the positive Z axis. The variances for the slope/intercept are provided in parenthesis after each fit parameter. The units for the slope and intercept are *GW*/*nT* and *GW*, respectively.

[32] Spatially dependent Joule heating during northward IMF is confined to the high-latitude dayside when the IMF magnitude is greater than 13.9 nT. When the IMF is southward, most of the Joule heating is constrained to the auroral oval, with increased heating during periods of increased IMF magnitude. During periods of increased IMF magnitude, there is a preference for heating in the postmidnight sector of the oval compared to the premidnight sector.

[33] **Acknowledgments.** We are grateful to Art Richmond for useful discussions.

[34] Shadia Rifai Habbal thanks Vytenis M. Vasyliunas and John M. Holt for their assistance in evaluating this paper.

References

Ables, S., B. Fraser, C. Waters, D. Neudegg, and R. Morris (1998), Monitoring cusp/cleft topology using Pc5 ULF waves, *Geophys. Res. Lett.*, *25*(9), 1507–1510.

André, M., H. Koskinen, L. Matson, and R. Erlandson (1988), Local transverse ion energization in and near the polar cusp, *Geophys. Res. Lett.*, *15*(1), 107–110.

André, M., G. Crew, W. Peterson, A. Persoon, C. Pollock, and M. Engebretson (1990), Ion heating by broadband low-frequency waves in the cusp/cleft, *J. Geophys. Res.*, *95*(A12), 20,809–20,823.

André, R., M. Pinnock, and A. Rodger (2000), Identification of the low-altitude cusp by Super Dual Auroral Radar Network radars: A physical explanation for the empirically derived signature, *J. Geophys. Res.*, *105*(A12), 27,081–27,094.

Baker, K. B., R. A. Greenwald, J. M. Ruohoniemi, J. R. Dudeney, M. Pinnock, P. T. Newell, M. E. Greensapn, and C.-I. Meng (1990), Simultaneous HF-radar and DMSP observations of the cusp, *Geophys. Res. Lett.*, *17*, 1869–1872.

Baker, K. B., J. R. Dudeney, R. A. Greenwald, M. Pinnock, P. T. Newell, A. S. Rodger, N. Mattin, and C.-I. Meng (1995), HF radar signatures of the cusp and low-latitude boundary layer, *J. Geophys. Res.*, *100*, 7671–7695.

Chun, F. K., D. J. Knipp, M. G. McHarg, J. R. Lacey, G. Lu, and B. Emery (2002), Joule heating patterns as a function of polar cap index, *J. Geophys. Res.*, *107*(A7), 1119, doi:10.1029/2001JA000246.

Codrescu, M. V., T. J. Fuller-Rowell, J. C. Foster, J. M. Holt, and S. J. Cariglia (2000), Electric field variability associated with the Millstone Hill electric field model, *J. Geophys. Res.*, *105*, 5265–5273.

Foster, J. C., J. P. St. Maurice, and V. J. Abreu (1983), Joule heating at high latitudes, *J. Geophys. Res.*, *88*, 4885–4896.

Fuller-Rowell, T. J., and D. S. Evans (1987), Height-integrated Pedersen and Hall conductivity patterns inferred from the TIROS-NOAA satellite data, *J. Geophys. Res.*, *92*, 7607–7618.

Germany, G. A., M. R. Torr, D. G. Torr, and P. G. Richards (1994), Use of FUV auroral emissions as diagnostic indicators, *J. Geophys. Res.*, *99*, 383.

Hardy, D. A., M. S. Gussenhoven, and E. Holeman (1985), A statistical model of auroral electron precipitation, *J. Geophys. Res.*, *90*, 4229–4248.

Innis, J. L., and M. Conde (2002), High-latitude thermospheric wind activity from Dynamics Explorer-2 wind and temperature spectrometer observations: Indications of a source region for polar cap gravity waves, *J. Geophys. Res.*, *107*(A8), 1172, doi:10.1029/2001JA009130.

Knipp, D. J., W. K. Tobiska, and B. Emery (2004), Direct and indirect thermospheric heating sources for solar cycles 21–23, *Sol. Phys.*, Oct.

Lu, G., A. D. Richmond, B. A. Emery, and R. G. Roble (1995), Magnetospere-ionosphere-thermosphere coupling: Effect of neutral winds on energy transfer and field-aligned current, *J. Geophys. Res.*, *100*, 19,643–19,659.

Matsuo, T., A. D. Richmond, and K. Hensel (2003), High-latitude ionospheric electric field variability and electric potential derived from DE-2 plasma drift measurements: Dependence on IMF and dipole tilt, *J. Geophys. Res.*, *108*(A1), 1005, doi:10.1029/2002JA009429.

Maynard, N., T. Aggson, E. Basinska, W. Burke, P. Craven, W. Peterson, M. Sugiura, and D. Weimer (1991), Magnetospheric boundary dynamics: DE 1 and DE 2 observations near the magnetopause and cusp, *J. Geophys. Res.*, *96*(A3), 3505–3522.

McHarg, M. G., J. V. Olson, and P. T. Newell (1995), ULF cusp pulsations: Diurnal variations and interplanetary magnetic field correlations with ground-based observations, *J. Geophys. Res.*, *100*(A10), 19,729–19,742.

Press, W. H., B. P. Flannery, S. A. Teukolsky, and W. T. Vetterling (1990), *Numerical Recipes: The Art of Scientific Computing (FORTRAN VERSION)*, pp. 504–505, Cambridge Univ. Press, New York.

Rich, F. J., M. S. Gussenhoven, and M. E. Greenspan (1987), Using simultaneous particle and field measurements to estimate Joule heat energy flow into the high latitude ionosphere, *Ann. Geophys.*, *5A*(6), 527–534.

Richmond, A. D. (1978), Gravity wave generation, propagation, and dissipation in the thermosphere, *J. Geophys. Res.*, *83*, 4131–4145.

Richmond, A. D., and Y. Kamide (1988), Mapping electrodynamic features of the high-latitude ionosphere from localized observations: Technique, *J. Geophys. Res.*, *93*, 5741–5759.

Richmond, A. D., and J. P. Thayer (2000), Ionospheric electrodynamics: A tutorial, in *Magnetospheric Current Systems*, *Geophys. Monogr. Ser.*, vol. 118, pp. 131–146, AGU, Washington, D. C.

Richmond, A. D., S. Matsushita, and J. D. Tarpley (1976), On the production mechanism of electric currents and fields in the ionosphere, *J. Geophys. Res.*, *81*, 547–555.

Roble, R. G., A. D. Richmond, W. L. Oliver, and R. M. Harper (1978), Ionospheric effects of the gravity wave launched by the September 18, 1974, sudden commencement, *J. Geophys. Res.*, *83*, 999–1009.

Shue, J. H., P. T. Newell, K. Liou, and C.-I. Meng (2001), Influence of interplanetary magnetic field on global auroral patterns, *J. Geophys. Res.*, *106*, 5913.

Thayer, J. P. (1998), Height-resolved Joule heating rates in the high-latitude E region and the influence of neutral winds, *J. Geophys. Res.*, *103*, 471–487.

Thayer, J. P., J. F. Vickery, R. A. Heelis, and J. B. Gary (1995), Interpretation and modeling of the high-latitude electromagnetic energy flux, *J. Geophys. Res.*, *100*, 19,715–19,728.

Weimer, D. R. (2001), An improved model of ionospheric electric potentials including substorm perturbations and application to the Geospace Environment Modelling November 24, 1996, event, *J. Geophys. Res.*, *106*, 407–416.

Wilson, C. T. (1969), Auroral infrasonic waves, *J. Geophys. Res.*, *74*(7), 1812–1836.

Wilson, C. T., R. D. Hunsucker, and G. R. Romick (1976), *An Auroral Infrasonic Substorm Investigation Using Chatanika Radar and Other Geophysical Sensors*, *Planet. Space Sci. Ser.*, vol. 24, pp. 1155–1175, Elsevier, New York.

F. Chun, D. Knipp, and M. McHarg, Department of Physics, U.S. Air Force Academy, 2354 Fairchild Drive, Suite 2A31, USAF Academy, CO 80840, USA. (matthew.mcharg@usafa.af.mil)

B. Emery and G. Lu, High Altitude Observatory, NCAR, Boulder, CO 80307, USA.

A. Ridley, Space Physics Research Laboratory, University of Michigan, Ann Arbor, MI 48109, USA.